AIChE

Using NMR Displacement Measurements to Probe CO_2 Entrapment in Porous Media

R. Hussain, T.R.R. Pintelon, J. Mitchell, and M.L. Johns
Dept. of Chemical Engineering and Biotechnology, University of Cambridge, Cambridge, CB2 3RA, UK

DOI 10.1002/aic.12401

Carbon dioxide sequestration in aquifers is seen as a potential climate change mitigation technique. One physical mechanism by which this could occur is capillary trapping of discrete pore-scale CO_2 bubbles (referred to as ganglia) in the pore space. Nuclear magnetic resonance (NMR) techniques were used to quantify the spatial distribution and pore environment of such CO_2 entrapment in a model porous medium (random glass bead packing). 3D images revealed a relatively macroscopically homogeneous CO_2 entrapment, even though the image resolution is insufficient to resolve individual CO_2 ganglia. Quantification of the pore environment of the CO_2 ganglia was achieved using NMR displacement propagators (displacement probability distributions), acquired both before and after CO_2 entrapment. Lattice Boltzmann (LB) simulations were used to facilitate interpretation of the propagator statistics by considering various pore environments in which CO_2 could become trapped. Comparison with the experimental data suggests that CO_2 is preferentially entrapped in comparatively larger pores. © 2010 American Institute of Chemical Engineers *AIChE J,* 57: 1700–1709, 2011
Keywords: CO_2 sequestration, NMR PFG, displacement propagators, capillary trapping, lattice Boltzmann

Introduction and Background

Carbon dioxide (CO_2) is a greenhouse gas which is emitted to the atmosphere from many different anthropogenic activities such as transport, industry, and electricity generation. According to the International Energy Agency,[1] in 2007, global CO_2 emissions totalled 29 billion metric tonnes. Against this backdrop, the geological sequestration or long-term storage of CO_2 in the subsurface has been put forward and widely researched as a potential mitigation technique for climate change. In particular, the storage of CO_2 in saline aquifers is of considerable interest, as such aquifers comprise the highest storage capacity for CO_2 of all geological formations.[2] The main processes by which CO_2 can be sequestered in aquifers usually involve the injection of a bulk CO_2 phase, which rises because of buoyancy and is trapped under a layer of suitable cap rock—a process known as hydrodynamic trapping. Other trapping mechanisms include solubility trapping, in which gradual subsurface CO_2 dissolution creates a local denser phase hence establishing convection currents, mixing[3] and mineral trapping, whereby CO_2 is converted into carbonate minerals such as calcite by reactions with the mineral/rock matrix.

An alternative trapping mechanism is retention of CO_2 in water-wet pore space as discrete gas pockets or bubbles (hereafter referred to as ganglia to be consistent with terminology used to describe the entrapment of nonaqueous phase liquids by the same physical process) through the action of capillary forces; this is referred to as residual trapping.[4] Such a mechanism might account for a residual gas saturation of up to 25%.[5] Note that such capillary trapping can be induced by water flooding following bulk CO_2 injection. Capillary trapping of CO_2 provides a very stable and rapid sequestration mechanism; how best to economically achieve

---

Correspondence concerning this article should be addressed to M.L. Johns at mlj21@cam.ac.uk.

this physical state is still open to debate.[2,6] Also of relevance is the analysis by Burton and Bryant[7] of a prototypical process in which captured CO_2 is dissolved in brine which is extracted from, and subsequently reinjected into, the target aquifer (known as "surface dissolution" trapping).

In the work presented here, we consider capillary or residual trapping of CO_2 in the pore space as ganglia, which occupy a small number of connected pores. Being predominately nonwetting under the conditions used in this work,[8] the CO_2 ganglia experience capillary forces that resist their transport through narrow pore necks. Where this net capillary force from all CO_2–water interfaces exceeds or equals the viscous forces imposed by superficial flow of the surrounding wetting fluid (water) and vertical buoyancy forces, the ganglia are trapped in the pore space of the porous medium. Significant simulation-based studies have appeared in the literature considering this capillary trapping mechanism.[9–12] We will consider the application of various nuclear magnetic resonance (NMR) techniques to characterise such CO_2 capillary trapping in a model porous media. To create residual CO_2 in the form of isolated ganglia, we flow carbonated brine through the porous media, a mechanism which is also relevant to "surface dissolution" trapping as discussed above. The NMR techniques used include both imaging of the water phase in the pore space and monitoring the influence of entrapped CO_2 on water flow characteristics, as probed by NMR pulsed field gradient (PFG) techniques in the form of displacement propagators. Such transport measurements are compared subsequently with simulations of the propagators using lattice Boltzmann (LB) techniques applied to various CO_2 entrapment scenarios. The LB method was used because of its uncomplicated implementation in simulating flow in complex porous media.[13] In this manner, we seek to investigate the pore morphology in which CO_2 becomes entrapped, and more specifically determine whether the CO_2 ganglia are entrapped preferentially in small pores (which provide more potential bubble nucleation sites, larger local pressure drops per unit length in general encouraging CO_2 ganglia formation and typically smaller pore necks providing larger capillary forces for trapping) or larger pores (which the nonwetting CO_2 will occupy preferentially occupy because of wettability effects). Note that the length scales involved (~10–100 μm) preclude the effective use of magnetic resonance imaging (MRI) to directly resolve individual ganglia of CO_2.

It is also important to note that recent studies appearing in the literature[14,15] have indicated that the injection of a dense, supercritical CO_2 phase can change the wetting properties of minerals found in subsurface rock at temperature, pressure and salinity conditions representative of deep subsurface storage. An increase in CO_2 wetting would undoubtedly have an effect on the amount of CO_2 retained because of hydrodynamic trapping as well on as the mechanism of capillary trapping.

The displacement propagator, $P(\zeta, \Delta)$, is the probability distribution of molecular displacements ζ averaged across the sample over the observation time interval, Δ. It is measured using PFG NMR techniques.[16] These techniques have been used to study fluid flow in a variety of porous media such as various forms of bead pack[17–21] and porous rock cores.[22–25] The ultimate applications of these studies have included biological perfusion, contaminated land cleanup, chemical reactor hydrodynamics and secondary and tertiary oil recovery.[20] Displacement propagators, as acquired by PFG NMR, have also been used to validate LB simulations of flow through porous media.[26–31] Advantages of PFG NMR include the ability to probe systems under flow nonintrusively by acquiring NMR signal directly from molecules in the flowing fluid without the need to inject tracer material, as well as the ability to observe the relative contribution of diffusion and advection to transport over different length and time scales. PFG NMR displacement propagators can also be used to probe structural changes in porous media, by comparing propagators before and after some modification to the pore space. A similar method to the one presented in this work was used by Johns et al.[23] to study changes in the permeability of rock cores because of polymer treatment as employed in the oil industry. Seymour et al.[32] and Graf von der Schulenburg et al.[33] have considered the effect of biofilm growth on liquid transport in model porous media based on the shape of acquired displacement propagators.

Experimental Methodology

Experimental setup

The model porous medium comprised a water-saturated bed of borosilicate glass beads (ballotini) of 100 ± 20 μm diameter packed randomly in a cylindrical Perspex column of length 69 mm and internal diameter 37 mm. The bead size was chosen because it gives a pore size similar to that of high-permeability sandstone rock.[34] Borosilicate glass ballotini were used because they exhibit smaller background magnetic field gradients due to magnetic susceptibility differences between solid surfaces and liquid, as compared with soda lime glass. The porosity, ε, of the packing was determined gravimetrically to be 0.385 ± 0.005. To prevent air bubbles forming in the column, the ballotini were poured into the column whilst it was fully submerged in deionised water. The NMR experiments detect the water in the pore space directly and no signal is obtained from the glass ballotini or container.

The bead pack was connected to a flow rig consisting of two Teledyne ISCO model 260D syringe pumps to provide continuous flow when required, see Figure 1. Two different solutions were pumped through at room temperature: "ordinary brine" (pH 8.0) consisting of a 2 wt% KCl aqueous solution and "carbonated brine" (pH 3.6). The pH was measured using a Corning pH meter. Brine was used (as opposed to deionised water) because it more accurately reflects the conditions in geologic saline aquifers. From CO_2 solubility data,[35] the saturation concentration of CO_2 in water under room conditions is 0.33 wt%. Using Henry's law and the pH data above, the concentration of CO_2 in the carbonated brine was estimated to be 0.65 wt% giving a degree of super saturation of approximately 2. It is acknowledged that under typical geological reservoir conditions, however, the solubility of CO_2 ranges between 2 and 12 wt% depending on the temperature, pressure, and salinity of the formation waters.[36]

NMR Measurements

All NMR measurements were performed using a Bruker Biospin AV85 spectrometer equipped with a 2 T horizontal-bore superconducting magnet, operating at a ^1H resonant

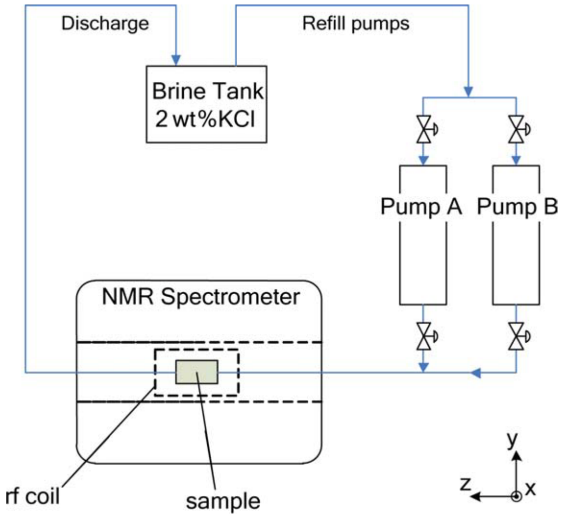

Figure 1. Experimental setup for pumping the fluids through the porous media sample.

The use of two pumps enables continuous flow via a refill-pump switch mechanism. [Color figure can be viewed in the online issue, which is available at wileyonlinelibrary.com.]

frequency of 85.18 MHz. A birdcage radio frequency (rf) coil of 55 mm inner diameter, and 204 mm length was used for signal excitation/detection. 1D spin-echo profiles were acquired along the sample in the z-(axial) direction, at a spatial resolution of 0.469 mm and a total acquisition time of 12 s. 2D spin-echo images in the x–y (transverse) plane of the sample were acquired with a data matrix size of 256 × 256 points (voxels) for a field of view of 40 mm × 40 mm, thereby giving a pixel resolution of 156 μm. The slice thickness used was 2 mm, and the recycle time (RT) used for imaging was 5 s resulting in a total image acquisition time of 1 h 25 min. 2D Images were acquired at several locations along the axis of the sample.

PFG NMR was used to acquire displacement propagators using both:

- A standard APGSTE (alternating pulsed gradient stimulated echo) pulse sequence based on the "13 interval" Cotts pulse sequence[35] (Figure 2a) that minimises the effect of background gradients arising from susceptibility differences between the fluids and the solid matrix and,
- A modified version of the APGSTE sequence incorporating a slice-selective 180° soft rf pulse (Figure 2b). A slice, from which signal was detected, was selected along the axis of the sample. Slice selection was added to the sequence to eliminate any signal contribution from the entry and exit regions of the column and to select a region of the sample with near uniform CO_2 entrapment to allow for an effective comparison with the simulations.

Propagators were acquired over a gradient (g) range of −10 to 10 G/cm with 32 equally spaced acquisition points. Observation times (Δ) of 100, 250, 500, and 750 ms were used. To accommodate this range and provide a suitable displacement acquisition window without aliasing, the gradient application time (δ) was varied from 7 to 2 ms. The RT used was 4.5 s resulting in a total acquisition time of 20 min per propagator.

Experiments performed

The experimental procedure used was as follows: the sample saturated with brine solution was placed in the NMR spectrometer and a 1D spin-echo profile was acquired, as well as 2D spin-echo images of slice thickness 2 mm centred at $z = 4.5$ mm, $z = 34.5$ mm and $z = 54.5$ mm.

Brine solution was then pumped through the sample at a volumetric flowrate (Q) of 20 ml/min. Displacement propagators were acquired at Observation times (Δ) of 100, 250, 500 and 750 ms with and without slice selection. The brine was then replaced with carbonated brine solution; Q was retained at 20 ml/min. Flow was maintained until no further CO_2 entrapment was evident based on the acquired 1D MRI profiles. The suite of NMR imaging (under no flow conditions) and displacement propagator experiments was then repeated. The position of the selected slice used for the displacement propagator acquisition was adjusted to a region of relatively homogeneous CO_2 entrapment informed by the acquired 1D MRI profiles. All propagator experiments were performed multiple times to ensure reproducibility.

Simulation Methodology

Displacement propagator simulations were performed using a LB platform to describe the flow field and a Lagrangian particle-tracking algorithm (also denoted as a directed random walk [DRW] algorithm) imposed on fluid "particles" or seeds migrating through the resultant flow field. This method is the same, essentially, as that used by Manz et al. (1999),[27] where further details of the methodology can be sourced. Subsequently, this simulation methodology has been used extensively in the literature in this capacity,[28,38–39] and features frequent favorable quantitative comparisons of simulated displacement propagators against corresponding experimental results.

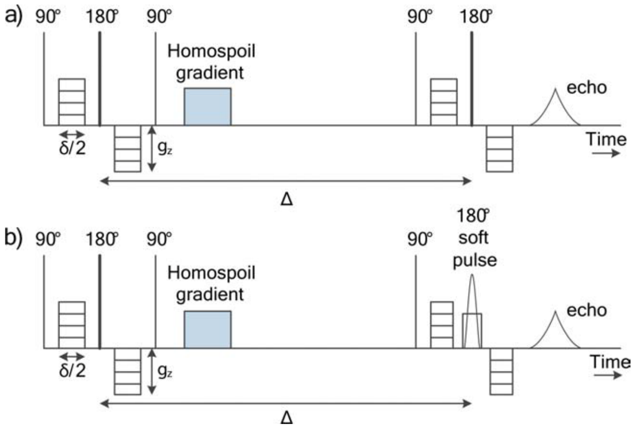

Figure 2. (a) APGSTE pulse sequence for displacement propagator acquisition; (b) Modified APGSTE pulse sequence with a 180° "gaussian" soft rf pulse used for slice-selective signal acquisition instead of the usual hard 180° rf pulse.

The NMR signal is acquired at the center of each echo. [Color figure can be viewed in the online issue, which is available at wileyonlinelibrary.com.]

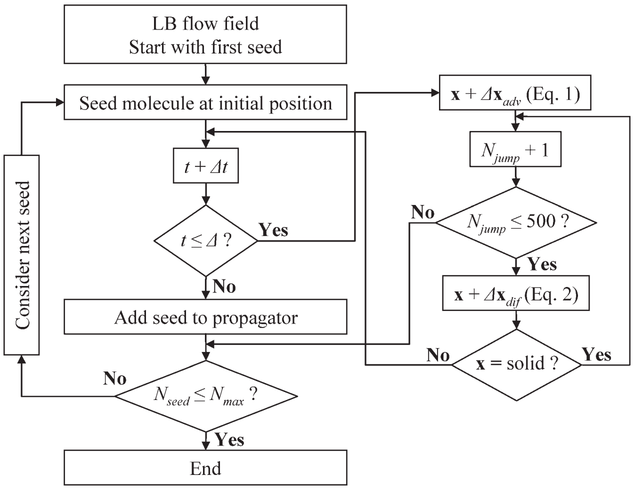

Figure 3. DRW algorithm used for displacement propagator simulations from LB flow fields.

The LB technique used is based on the modified lattice Bhatnagar-Gross-Krook method.[40] The chosen mean pore velocity of 0.81 mm s^{-1} was set equal to that used in the experiments. Displacement propagators were then simulated using the DRW algorithm that takes into account both diffusive and advective processes experienced by fluid molecules in the porous bed over the observation time, Δ. The observation time was divided into small computational time steps, *dt*, where *dt* specifies the size of the advective and diffusive increments as defined by:

$$\Delta\mathbf{x}_{\mathrm{adv}} = \mathbf{v}dt \tag{1}$$

and

$$\Delta\mathbf{x}_{\mathrm{dif}} = \sqrt{2D_0 dt} \tag{2}$$

where v is the interpolated velocity from the surrounding grid nodes (as determined using LB), and D_0 is the self-diffusivity of water at 21°C – 2×10^{-9} m^2 s^{-1}. The advection step $\Delta\mathbf{x}_{\mathrm{adv}}$ at any given position is thus calculated for each coordinate direction. The diffusion step size $\Delta\mathbf{x}_{\mathrm{dif}}$ is calculated randomly within a Gaussian probability window for which the root mean squared average of the diffusive jump sizes in each coordinate direction is given by Eq. 2. The total displacement of the "particle" during *dt* is given by the vector sum of $\Delta\mathbf{x}_{\mathrm{adv}}$ and $\Delta\mathbf{x}_{\mathrm{dif}}$. The overall displacement of each seed during Δ is defined as the vector sum of all individual $\Delta\mathbf{x}_{\mathrm{adv}}$ and $\Delta\mathbf{x}_{\mathrm{dif}}$ increments for that "particle"; collation of all "particle" displacements results in the final displacement propagator. All voxels in the image domain are seeded with such fluid particles. A flow chart summarising the key operations and decisions of the DRW algorithm is shown in Figure 3. If a fluid particle is transported to a position in the simulation mask that corresponds to solid packing then it will undergo a number of diffusive steps (denoted as N_{jump} in Figure 3) up to a maximum of 500, to diffuse back into the fluid-occupied pore space so that it can undergo another advective step. This provides a computationally cheap method of simulating collisions between the fluid particles and the solid packing.

A 3D MRI image of a monodisperse bead packing was used to provide a lattice for the simulation. This image was binary gated to differentiate the fluid occupied pore space from the solid matrix. The original image consisted of 3-mm diameter beads packed randomly in a 45-mm inner diameter column. The image consisted of 256^3 voxels, the length-scale of these was scaled such that the mean bead diameter matched that employed experimentally (100 μm). This lattice generation procedure was necessary because it is not possible to image the 100-μm bead diameter packing at sufficient resolution to provide the required simulation lattice. A similar simulation lattice generation procedure has been successfully used before.[39] Sample transverse and axial 2D slices extracted from the 3D simulation lattice are shown in Figures 4a and b. This was the largest simulation domain computationally possible with our resources, presenting a

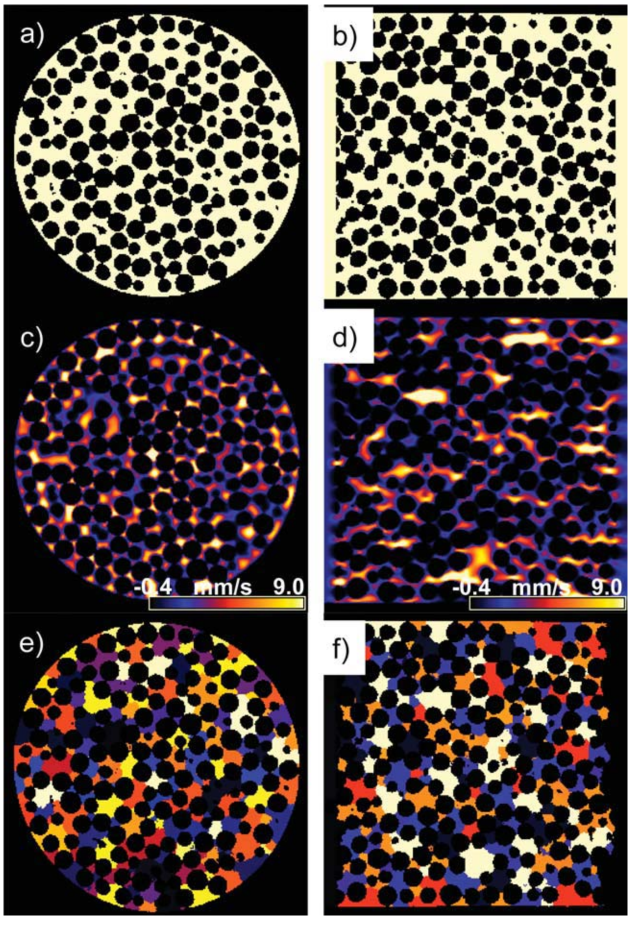

Figure 4. (a) Transverse and (b) axial slices extracted from the simulation lattice.

Pore space is shown in beige. The corresponding velocity images after application of the LB simulation method are shown in (c) and (d), respectively. Velocity is shown in the superficial (axial) flow direction. (e) and (f) show the partitioning of the pore space into individual pores in the same slices as above, prior to allocation of selected pores as being 'filled' by CO$_2$. [Color figure can be viewed in the online issue, which is available at wileyonlinelibrary.com.]

column-to-bead diameter ratio of 16; generally a ratio of 10 is considered sufficient to minimise wall packing effects.[41] Nevertheless the simulation domain is necessarily approximately 24 times smaller than the packed column used experimentally for propagator generation. The corresponding velocity images generated by application of LB are shown in Figures 4c and d for the corresponding slices in (a) and (b)—the component in the superficial flow direction has been plotted.

Different pore environments for CO_2 entrapment were then considered. A pore thinning algorithm developed by Baldwin et al. (1996)[42] was used to divide the void space in the image into discrete pores where the boundaries between pores are defined as local minima in hydraulic radius (known as ''pore necks''). The algorithm is a variant of morphological thinning, a technique commonly used in image analysis for reducing an image down to a skeleton; pore centres are identified as local maxima in the assigned thinning layer value. This method enables various statistics such as pore size distribution to be obtained from the pore partitioned data. Moreover, the generalised definition of a pore used in the algorithm makes the method valid for any image of a 3D porous medium. Figures 4e and f shows this pore allocation for the corresponding slices shown in (a) and (b), respectively. Different ''rules'' were then applied in terms of allocating pores that became occupied by CO_2. CO_2 is a nonwetting fluid with respect to water in the bead packs; and thus, will preferentially occupy the larger pores. However, smaller pores will provide more surface area for ganglia formation from the carbonated brine solution and higher local pressure drops per unit length possibly encouraging local bubble formation. Smaller pores are also more likely to be associated with smaller pore necks which will impose larger capillary forces for ganglia entrapment. Thus using the known experimental CO_2 gas saturation from experiments, pores in the simulation lattice were switched from being water saturated to being occupied by CO_2 until the % value for the experimental CO_2 gas saturation was reached for the following scenarios:

Scenario 1—the smallest pores fill with CO_2 preferentially,

Scenario 2—the largest pores fill with CO_2 preferentially and,

Scenario 3—random allocation of pores to be filled with CO_2.

LB flow fields were then recalculated treating CO_2-occupied pores effectively as solids and the propagators resimulated.

Results and Discussion

Experimental

Figure 5a shows displacement propagators acquired for ordinary brine, using both the standard and slice selective APGSTE pulse sequences, see Figures 2a and b, respectively. The soft pulse employed in the slice selective APGSTE pulse sequences excited a slice of thickness 14 mm centred at a position of 34.5 mm along the total sample length of 69 mm, i.e., approximately near the middle of the sample. The small peak centred on zero mean displacement in Figure 5a for the full sample propagator is associated with entrance and exit effects of the sample and is eliminated by the slice selection. Apart from this minor peak, there is excellent agreement between the two methods indicating that transport in the selected region is indicative of bulk behaviour. Figure 5b shows the evolution in the slice selective propagators as a function of Δ, the observation time. As Δ increases, the displacement propagator evolves from a skewed exponential shape to a Gaussian shape centered on the mean displacement, as observed frequently in the literature.[43] The experimental mean displacement, $\langle\zeta\rangle_m$, was determined for each of the propagators shown in Figure 5b and compared with the predicted mean displacement, $\langle\zeta\rangle_0$, predicted based on the known porosity, volumetric flowrate, and Δ. This produced a ratio $\langle\zeta\rangle_m/\langle\zeta\rangle_0$ of 1.11, 1.1, 1.07, and 1.07 for Δ of 100, 250, 500, and 750 ms, respectively. A systematic error might arise from the porosity in the selected region being slightly different to that measured for the bulk packing. Nevertheless these values are broadly consistent with those of Scheven et al. (2005)[24] for a similar bead pack, where an average $\langle\zeta\rangle_m/\langle\zeta\rangle_0$ of 1.05 was reported. This discrepancy may be explained by the presence of surface signal relaxation effects, which reduces the relative contribution of ''slow'' molecules, located near or on relaxing pore walls, to the propagator measurement—thus artificially enhancing the measured mean displacement.

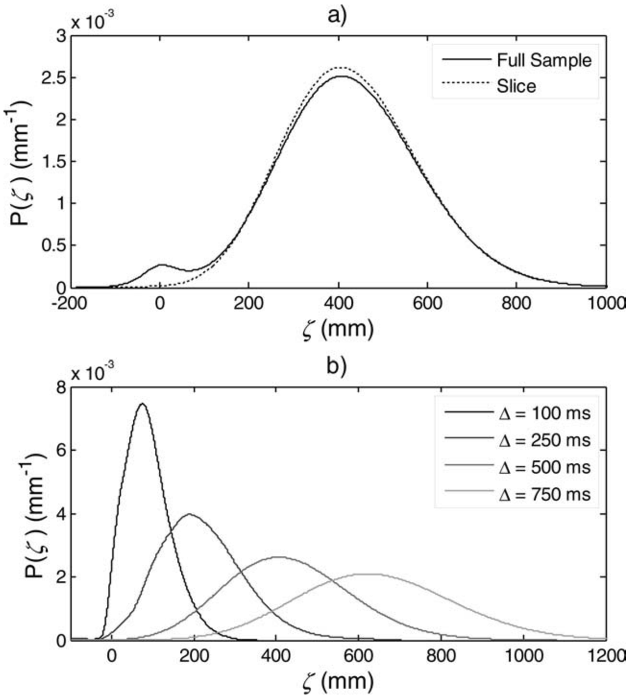

Figure 5. Displacement propagators corresponding to an observation time of 500 ms acquired without and with slice-selection.

Slice selection was introduced using the pulse sequence shown in Figure 2(a) and excited a region 14-mm thick centred in the middle of the column at a distance of 34.5 mm from the inlet (along a total column length of 69 mm). (b) The evolution in the propagator shape with increasing Δ.

1D NMR profiles of the sample were taken along the axial direction both before and after carbonated brine flowed through the sample, these are shown in Figure 6. The

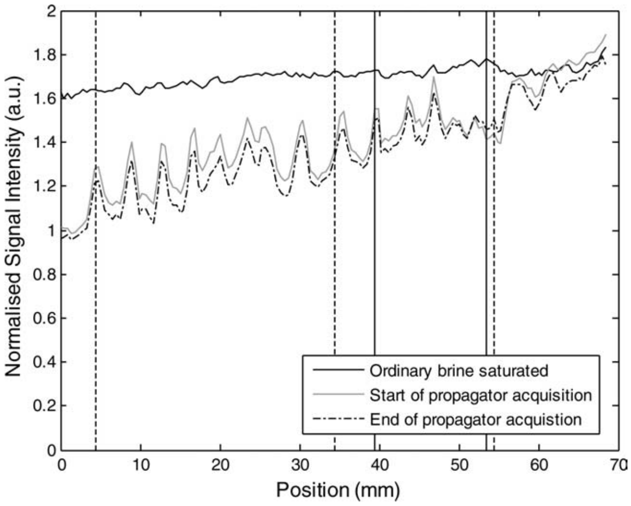

Figure 6. 1D NMR water content profiles across the sample in the axial-direction before and after flowing carbonated brine through the packing.

The solid vertical lines indicate the boundaries of the sample slice used for propagator measurements. The dashed vertical lines indicate the positions of the 2D cross-sectional images presented in Figure 9.

profiles were normalised using a homogeneous sample of identical bulk dimensions to the porous media flow cell, consisting of water doped with 0.5 g/L Mn^{2+} ($T_1 = 50$ ms). This corrected for any r.f. inhomogeneities or gradient nonlinearities and enabled the determination of calibrated axial brine-saturation profiles for the column. The profile acquisition parameters were selected to minimise any significant signal relaxation. Figure 6 shows that there is a reduction in water saturation as expected after flowing the carbonated brine through the sample, with more CO_2 being trapped near the inlet. This axial trapping variation was reproducible and tended to increase when an increased flowrate was used.

To provide a sensible comparison with simulations based by necessity on a smaller lattice, propagators were acquired using slice selection to detect signal only from the region between the solid black lines in Figure 6. CO_2 entrapment in this region was seen to be relatively homogeneous in an axial direction, and the average reduction in water saturation was 13% after entrapment. A 1D profile was also acquired at the end of propagator acquisition (shown in Figure 6) and revealed minimal differences from that acquired before propagator acquisition. This confirmed that minimal change had occurred in CO_2 spatial distribution as a consequence of propagator acquisition. Figure 6 also reveals obvious oscillations in the signal intensity with a period of approximately 3.8 mm equivalent to 38 bead diameters. The reason for this is unclear at present, although the oscillation is reproducible

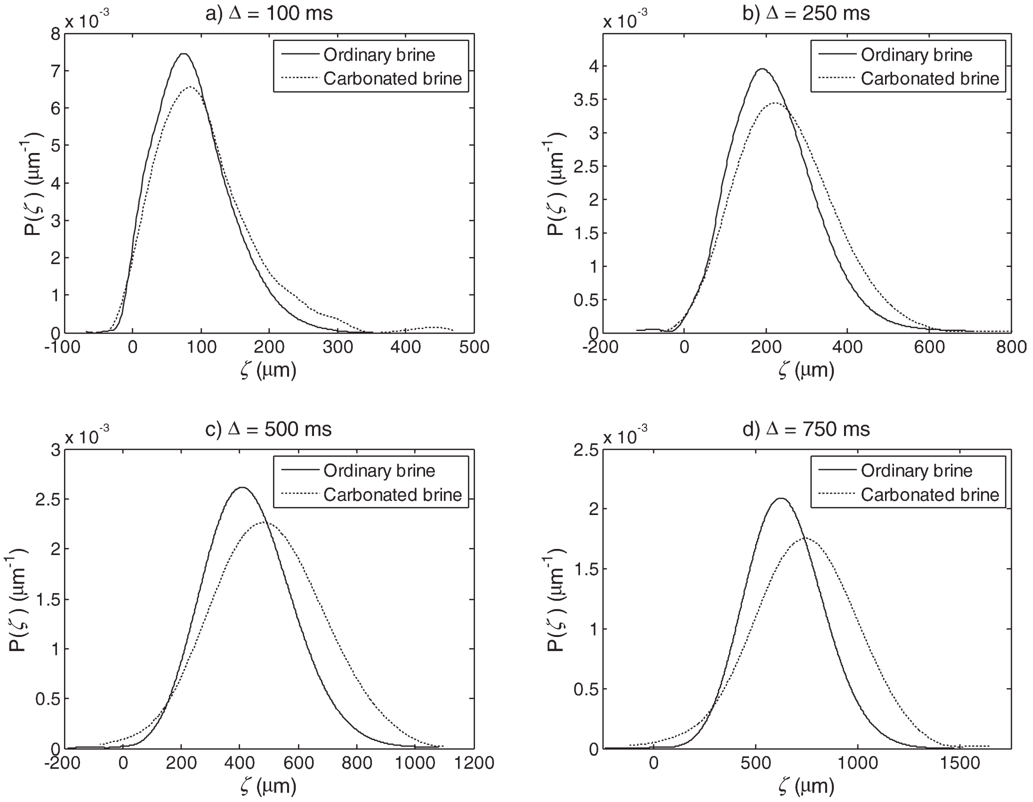

Figure 7. (a)–(d) ^{1}H APGSTE displacement propagators for ordinary and carbonated brine at a flowrate of 20 ml/min through the column filled with 100 μm ballotini.

A 180° soft rf pulse was added to the APGSTE pulse sequence, which selected a slice of thickness 14 mm centred on $z = 34.5$ mm and $z = 46$ mm (along a sample of length 69 mm) for ordinary and carbonated brine, respectively.

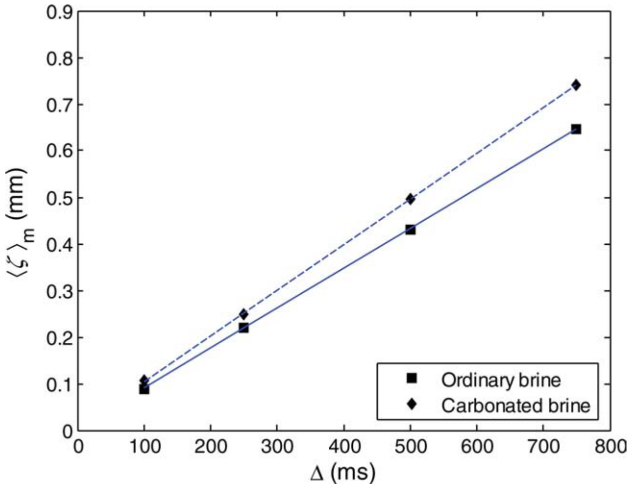

Figure 8. Measured mean displacements plotted against observation time with best-fit lines for ordinary and carbonated brine propagators, respectively.

[Color figure can be viewed in the online issue, which is available at wileyonlinelibrary.com.]

and occurs over a broad range of flowrates; it will be explored further in future work. However, the region selected for propagator acquisition contains relatively minimal oscillation in signal intensity.

Figure 7 shows the slice-selective displacement propagators obtained for ordinary and carbonated brine solution flowing through the column at 20 ml/min. Overall, the propagators for both cases are similar, although the differences that do exist are reproduced consistently across all values of Δ. In particular, the larger mean displacements observed in the carbonated brine propagators are consistent with CO_2 being trapped in the pore space; and therefore reducing the available cross sectional area for flow, which results in a greater interstitial velocity. These mean displacements, $\langle \zeta \rangle_m$, obtained from Figure 7 are shown in Figure 8. The relationship between $\langle \zeta \rangle_m$ and Δ for the two sets of propagators is seen to be linear in both cases, as expected. From the gradients of the lines of best fit in Figure 8, the reduction in pore space available for the flow of brine solution was calculated—this produced a value of 12.7% in good agreement with the 13% determined from the 1D profile data in Figure 6. Hence, the pore space available for flow of brine solution was reduced by 13% in all post-CO_2 entrapment simulations.

To check for any bulk trapping of the CO_2, 2D images with a slice thickness of 2 mm were taken at distances of 4.5 mm, 34.5 mm, and 54.5 mm along the axis of the 69-mm long column. The 2D images were also normalised using the homogenous phantom sample described earlier, to correct for rf inhomogenieties and gradient nonlinearities and hence enable quantitative comparison of the images. Difference maps of the two images acquired before and following CO_2 entrapment sets are shown in Figure 9; these have been converted into a % reduction in water saturation or content. From the 1D profiles shown in Figure 6, it is clear that the CO_2 is trapped preferentially near the sample inlet, this is also evident for the 2D images in Figure 9. Figure 9 also shows that the trapped CO_2 occurs throughout the entire column cross-section with a slight preference for the upper regions of the cell, due presumably to buoyancy effects. These images are consistent with the CO_2 ganglia locally occupying a small integer number of connected pores; large regions of CO_2-occupied pore space are not observed. This is consistent with the simulation lattices and CO_2 entrapment scenarios simulated.

Simulations

The simulated LB flow field in the chosen lattice (Figure 4) was then used to simulate displacement propagators, which were then compared with the experimental displacement propagators for ordinary brine solution. This comparison is shown in Figure 10. There is reasonable agreement between experimental and simulation results consistent with previous publications.[28,38–40] The simulated propagators are slightly broader (i.e., have a larger second moment) than the corresponding experimental propagators. We speculate this difference to be a consequence of the significantly smaller column-diameter to particle diameter ratio used for the simulations compared with that in the actual column. As such, the displacements determined from the necessarily smaller simulation lattice are influenced more heavily by flow heterogeneities because of the column wall.

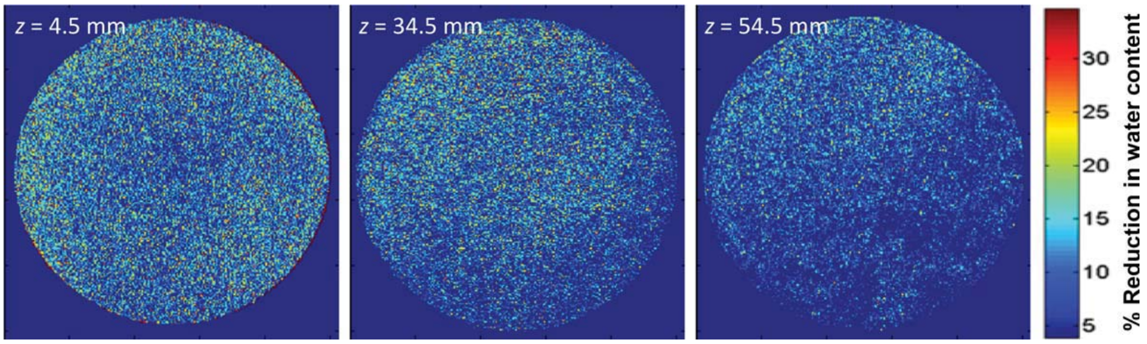

Figure 9. Difference map of 2D image intensity of sample cross-section before and after CO_2 bubble or ganglia formation in the pore space.

As such it represents the % local reduction in water saturation. [Color figure can be viewed in the online issue, which is available at wileyonlinelibrary.com.]

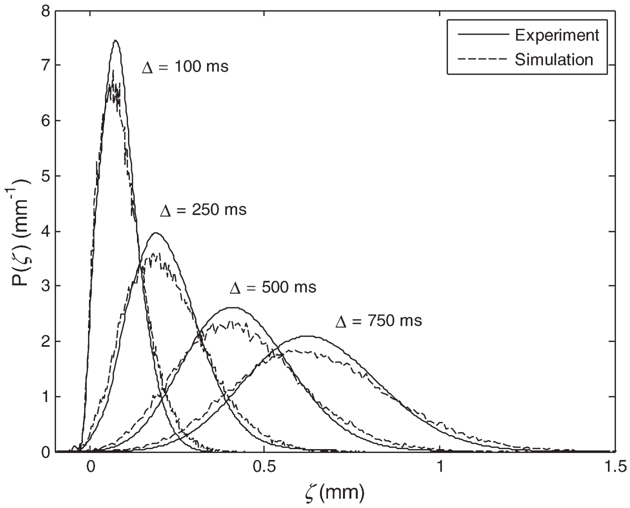

Figure 10. Comparison between experimental and simulated propagators for water flowing through a packing of 100 μm borosilicate ballotini at 20 ml/min at different observation times Δ.

The propagators simulated for the three scenarios for CO_2 entrapment are shown in Figure 11, along with the simulated propagators from the original unmodified simulation lattice. In all cases, the volumetric flowrate through the lattices was kept constant and consistent with the pore velocity of the corresponding experimental scenario. After CO_2 entrapment, there is an increase in mean displacement as expected and a broadening of the displacement peaks occurs for all scenarios considered. There are subtle differences between scenarios 1 and 2. The blocking of smallest pores in scenario 1 produces a more prominent stagnant peak at all observation times. This suggests that occupation of the smallest pores has the greatest effect on pore space connectivity and the creation of dead volume. Note that with respect to the corresponding experimental data in Figure 7, no significant peak is observed around zero displacement. The results for scenario 3 (blocking of random pores) appear to be in between those for scenarios 1 and 2, which is to be expected given that scenario 3 effectively represents a random combination of small and large pores occupied by CO_2.

To provide a more quantitative comparison of the simulations and the experiments, the ratio of the standard deviation of the carbonated brine propagators, σ_1, to the standard deviations of the ordinary brine propagators, σ_2 was calculated. The standard deviations were calculated using the definition:

$$\sigma = \sqrt{\zeta_2' - \zeta_1'^2} \tag{3}$$

where ζ_1' and ζ_2' are the first and second raw moments of the displacement propagator, respectively. The equivalent $\sigma_{1/}\sigma_2$ ratio was determined for the experimental data. The resultant ratio data for both the simulations and the experiments is plotted in Figure 12. The data for scenario 3 falls in between scenarios 1 and 2, as expected. The best agreement with the experimental data in Figure 12 is produced by scenario 2, where CO_2 entrapment occurs in the largest pores. Discrepancies

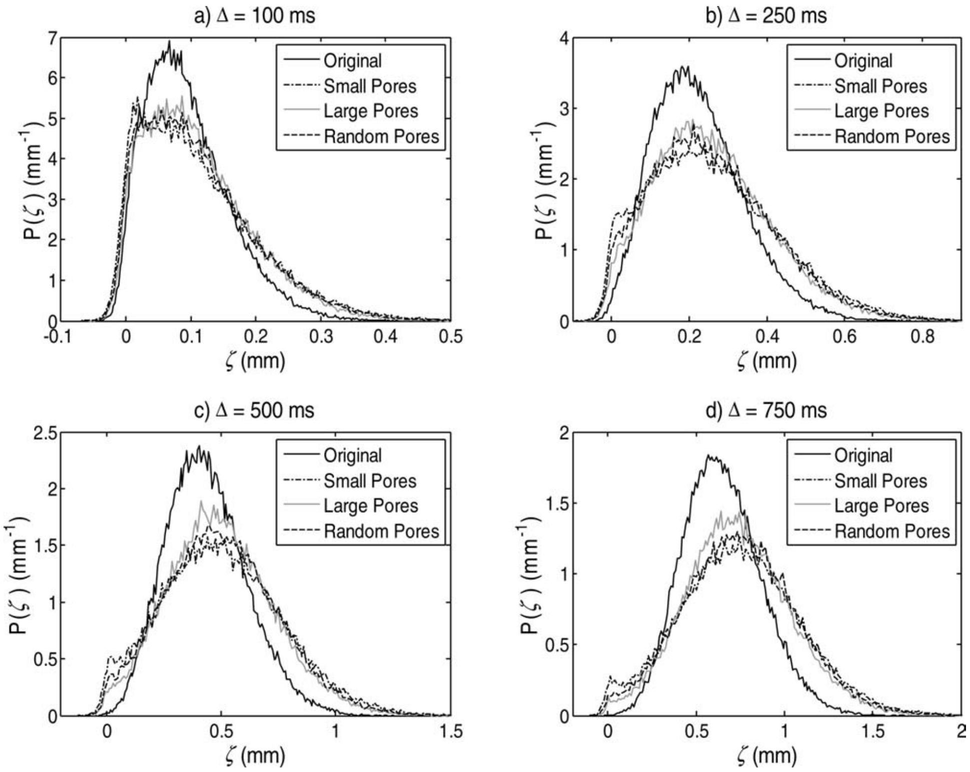

Figure 11. (a)–(d) Displacement propagators simulated on the original 256^3 simulation lattice and on the modified lattice with 13% of the pore space assigned to be CO_2 according to the three scenarios outlined in the text.

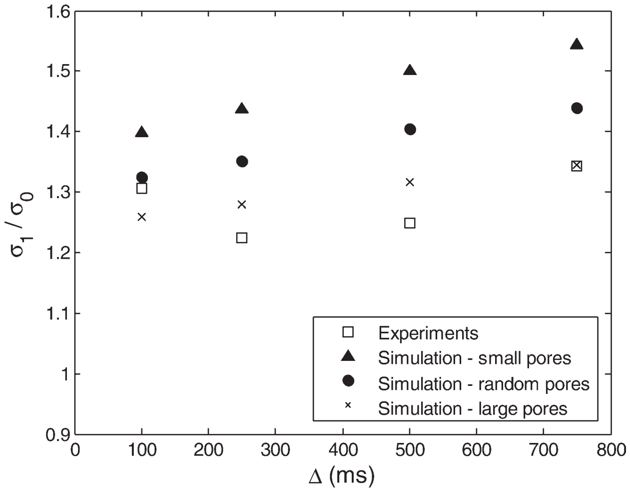

Figure 12. Ratio of standard deviations of displacement propagators before and after pore space modification by CO_2 entrapment for different observation times, Δ; comparison between experiments and simulations is shown.

between scenario 2 and the experimental σ_1/σ_2 ratio nevertheless are evident. These probably arise from several potential contributions, including the use of the smaller simulation lattice as discussed previously, the fact that the CO_2 might only preferentially occupy larger pores and not simply all the largest pores as assumed in the simulations, and the fact that in the experiments, CO_2 will only partially occupy many pores, whereas in the simulations full individual pore occupancy is assumed. Notwithstanding, we conclude from the results in Figure 12 that the CO_2 ganglia preferentially form in larger pores. This methodology will also potentially prove useful in terms of estimating the amount of CO_2 entrapment in rock cores.

Conclusions

Displacement propagators were acquired for brine flowing through a model porous medium (packed bed of glass ballotini) both before and after CO_2 entrapment in the pore space of the medium. These propagators were acquired using a slice selective APGSTE NMR pulse sequence for a range of observation times, Δ, which enabled selective signal detection from an axial region of the medium with relatively homogeneous CO_2 entrapment (average of 13% of the available pore space), as revealed by 1D NMR profiles of the column used. 2D NMR images revealed relatively homogeneous CO_2 entrapment across the cell cross-section with no large gas-filled regions. Analysis of the displacement propagators showed that the effective porosity of the column occupied by water was reduced by 12.7% as a consequence of CO_2 entrapment. This was in good agreement with the reduction in water saturation observed in the 1D NMR profiles. Interpretation of the differences in the propagators without and with CO_2 entrapment was facilitated by LB flow and propagator simulations applied to a model lattice. Different scenarios for CO_2 entrapment were considered in the simulations with occupation of the largest pores producing best agreement with the experimental data. Hence, we have been able to explore the pore characteristics of where CO_2 ganglia are most likely to form during entrapment. This work used a 3D realistic porous medium which was opaque and did not permit direct imaging of the CO_2 ganglia.

In this article, we have demonstrated the applicability of combining NMR experimental techniques (displacement propagators and 1D profiles) with LB flow and propagator simulations to gain insight into a porous medium where modifications are occurring to the pore space because of the capillary trapping of CO_2. This approach can now be extended to systems that more accurately reflect conditions in sub-surface aquifers such as higher temperatures and pressures and the use of real sandstone rock cores. Different experimental mechanisms to encourage CO_2 entrapment will also be explored and the LB simulation methodology extended to two-phase flow such that local CO_2 ganglia entrapment can be directly predicted.

Acknowledgments

The authors thank Dr Andy Sederman for supplying the MRI structural image used to create the simulation lattice. R.H. and T.R.R.P. thank the EPSRC (EP/E012205/1) and J.M. thanks Schlumberger Cambridge Research for financial support.

Notation

A = cross sectional area of the sample
D_0 = diffusion coefficient
$\mathrm{d}t$ = lattice Boltzmann timestep
g = strength of applied magnetic field gradient
N_{jump} = number of diffusive steps
N_{max} = sotal number of seeded voxels
N_{seed} = seeded voxel number
ΔP = pressure drop
Q = volumetric flowrate
RT = recycle time
t = time duration
T_1 = spin-lattice relaxation constant
T_2 = spin-spin relaxation constant
T_2^* = apparent spin-spin relaxation constant
u_{p} = mean pore velocity
v = Lattice Boltzmann velocity
$\Delta\mathbf{x}_{\mathrm{adv}}$ = advection step length
$\Delta\mathbf{x}_{\mathrm{dif}}$ = diffusion step length

Greek letters

Δ = PFG NMR observation time
δ = gradient pulse duration
ε = porosity
$\varepsilon_{\mathrm{eff}}$ = effective porosity
ζ = displacement
ζ_1 = first raw moment of displacement propagator
ζ_2 = second raw moment of displacement propagator
$\langle\zeta\rangle_{\mathrm{m}}$ = measured mean displacement
$\langle\zeta\rangle_0$ = expected mean displacement
σ = standard deviation
τ = echo time

Literature Cited

1. International Energy Agency. *CO_2 Emissions From Fuel Combustion: Highlights* (2009 Edition). Paris: International Energy Agency, 2009.
2. Metz B, Davidson O, de Coninck HC, Loos M, Meyer LA, editors. *IPCC Special Report on Carbon Dioxide Capture and Storage*

Prepared by Working Group III of the Intergovernmental Panel on Climate Change. Cambridge, UK: Cambridge University Press, 2005.

3. Ennis-King J, Paterson L. Role of convective mixing in the long-term storage of carbon dioxide in deep saline formations. *SPE J*. 2005;10:349–356.
4. Bachu S, Gunter WD, Perkins EH. Aquifer disposal Of CO_2—hydrodynamic and mineral trapping. *Energy Conversion Manag*. 1994;35:269–279.
5. Holtz MH. Residual gas saturation to aquifer influx: a calculation method for 3-D computer reservoir model construction. SPE Paper 75502, presented at the SPE Gas Technologies Symposium, Calgary, Canada, 2002.
6. Saadatpoor E, Bryant SL, Sepehrnoori K. New Trapping Mechanism in Carbon Sequestration. *Transport in Porous Media*. 2010;82:3–17.
7. Burton M, Bryant SL. Eliminating buoyant migration of sequestered CO_2 through surface dissolution: implementation costs and technical challenges. *SPE Reservoir Eval Eng*. 2009;12:399–407.
8. Dickson JL, Gupta G, Horozov TS, Binks BP, Johnston KP. Wetting phenomena at the CO_2/water/glass interface. *Langmuir*. 2006;22: 2161–2170.
9. Obdam A, van der Meer L, May F, Kervevan C, Bech N, Wildenborg A. *Effective CO_2 storage capacity in aquifers, gas fields, oil fields and coal fields*. Amsterdam: Elsevier Science Bv, 2003.
10. Kumar A, Ozah R, Noh M, Pope GA, Bryant S, Sepehrnoori K, Lake LW. Reservoir simulation of CO_2 storage in deep saline aquifers. *SPE J*. 2005;10:336–348.
11. Lin CK. Algorithm for determining optimum sequestration depth of CO_2 trapped by residual gas and solubility trapping mechanisms in a deep saline formation. *Geofluids*. 2008;8:333–343.
12. Juanes R, MacMinn CW, Szulczewski ML. The footprint of the co_2 plume during carbon dioxide storage in saline aquifers: storage efficiency for capillary trapping at the basin scale. *Transport in Porous Media*. 2010;82:19–30.
13. Ferreol B, Rothman, DH. Lattice-Boltzmann simulations of flow through Fontainebleau sandstone. *Transport in Porous Media*. 1995;20:3–20.
14. Stejskal EO, Tanner JE. Spin diffusion measurements: spin echoes in the presence of a time-dependent field gradient. *J Chem Phys*. 1965;42:288–292.
15. Chiquet P, Broseta D, Thibeau, S. Wettability alteration of caprock minerals by carbon dioxide. *Geofluids*. 2007;7:112–122.
16. Chalbaud C, Robin M, Lombard J-M, Egermann P, Bertin H. Interfacial tension measurements and wettability evaluation for geological CO_2 storage. *Adv Water Res*. 2009;32:98–109.
17. Lebon L, Leblond J, Hulin JP. Experimental measurement of dispersion processes at short times using a pulsed field gradient NMR technique. *Phys Fluids*. 1997;9:481–490.
18. Sederman AJ, Johns ML, Alexander P, Gladden LF. Visualisation of structure and flow in packed beds. *Magn Reson Imaging*. 1998;16: 497–500.
19. Britton MM, Graham RG, Packer KJ. NMR relaxation and pulsed field gradient study of alginate bead porous media. *J Magn Reson*. 2004;169:203–214.
20. Scheven UM, Seland JG, Cory DG. NMR propagator measurements on flow through a random pack of porous glass beads and how they are affected by dispersion, relaxation, and internal field inhomogeneities. *Phys Rev E*. 2004;69:021201.
21. Codd SL, Altobelli SA. A PGSE study of propane gas flow through model porous bead packs. *J Magn Reson*. 2003;163:16–22.
22. Packer KJ, Stapf S, Tessier JJ, Damion RA. The characterisation of fluid transport in porous solids by means of pulsed magnetic field gradient NMR. *Magn Reson Imaging*. 1998;16:463–469.
23. Johns ML, Sederman AJ, Gladden LF, Wilson A, Davies S. Using MR techniques to probe permeability reduction in rock cores. *AIChE J*. 2003;49:1076–1084.
24. Scheven UM, Verganelakis D, Harris R, Johns ML, Gladden LF. Quantitative nuclear magnetic resonance measurements of preasymptotic dispersion in flow through porous media. *Phys Fluids*. 2005;17: 117107.
25. Mitchell J, Sederman A, Fordham EJ, Johns ML, Gladden LF. A rapid measurement of flow propagators in porous rocks. *J Magn Reson*. 2008;191:267–272.
26. Maier RS, Kroll DM, Kutsovsky YE, Davis HT, Bernard RS. Simulation of flow through bead packs using the lattice Boltzmann method. *Phys Fluids*. 1998;10:60–74.
27. Manz B, Gladden LF, Warren PB. Flow and dispersion in porous media: lattice-Boltzmann and NMR studies. *AIChE J*. 1999;45: 1845–1854.
28. Mantle MD, Sederman AJ, Gladden LF. Single- and two-phase flow in fixed-bed reactors: MRI flow visualisation and lattice-Boltzmann simulations. *Chem Eng Sci*. 2001;52:523–529.
29. Sullivan SP, Sederman AJ, Johns ML, Gladden LF. Verification of shear-thinning LB simulations in complex geometries. *J Nonnewtonian Fluid Mech*. 2007;143:59–63.
30. Hunter MW, Jackson AN, Callaghan PT. Nuclear magnetic resonance measurement and lattice-Boltzmann simulation of the nonlocal dispersion tensor *Phys Fluids*. 2010;22:027101.
31. Graf von der Schulenburg DA, Paterson-Beedle M, Macaskie LE, Gladden LF, Johns ML. Flow through an evolving porous media—compressed foam. *J Mater Sci*. 2007;42:6541–6548.
32. Seymour JD, Gage JP, Codd SL, Gerlach R. Anomalous fluid transport in porous media induced by biofilm growth. *PRL*. 2004;93: 198103.
33. Graf von der Schulenburg DA, Akpa BS, Gladden LF, Johns ML. Non-invasive mass transfer measurements in complex biofilm-coated structures. *Biotechnol Bioeng*. 2008;101:602–608.
34. Mitchell J, Chandrasekera TC, Johns ML, Fordham E, Gladden LF. Nuclear magnetic resonance relaxation and diffusion in the presence of internal gradients. *Phys Rev E*. 2010;81:026101.
35. Lewis RJ, editor. *Hawley's Condensed Chemical Dictionary*, 14th ed. New York: John Wiley & Sons, 2002.
36. Bachu S, Adams JJ. Sequestration of CO_2 in geological media in response to climate change: capacity of deep saline aquifers to sequester CO_2 in solution. *Energy Conversion Manag*. 2003;44: 3151–3175.
37. Cotts RM, Hoch MJR, Sun T, Markert JT. Pulsed field gradient stimulated echo methods for improved NMR diffusion measurements in heterogeneous systems. *J Magn Reson*. 1989;83:252–266.
38. Harris RJ, Sederman AJ, Mantle MD, Crawshaw J, Johns ML. A comparison of experimental and simulated propagators in porous media using confocal laser scanning microscopy, lattice Boltzmann hydrodynamic simulations and nuclear magnetic resonance *Magn Reson Imaging*. 2005;23:355–357.
39. Creber SA, Pintelon TRR, Johns ML. Quantification of the velocity acceleration factor for colloidal transport in porous media using NMR. *J Colloid Interface Sci*. 2009;339:168–174.
40. He XY, Luo LS. Lattice Boltzmann model for the incompressible Navier-Stokes equation. *J Stat Phys*. 1997;88:927–944.
41. Delgado J. A critical review of dispersion in packed beds. *Heat Mass Transf*. 2006;42:279–310.
42. Baldwin CA, Sederman AJ, Mantle MD, Alexander P, Gladden LF. Determination and characterisation of the structure of a pore space from 3D volume images. *J Colloid Interface Sci*. 1996;181: 79–92.
43. Scheven UM, Sen PN. Spatial and temporal coarse graining for dispersion in randomly packed spheres. *Phys Rev Lett*. 2002;89: 254501/1–4.

Manuscript received Jun. 18, 2010, and revision received Aug. 2, 2010.